JETIR.ORG

ISSN: 2349-5162 | ESTD Year : 2014 | Monthly Issue



JOURNAL OF EMERGING TECHNOLOGIES AND INNOVATIVE RESEARCH (JETIR)

An International Scholarly Open Access, Peer-reviewed, Refereed Journal

Evaluation of Photon Shielding Parameters in NiCuFe₂O₄ and NiMgFe₂O₄ Nanoparticles.

Kalidas B. Gaikwada*

^{a*}Department of Physics, Dr. Babasaheb Ambedkar Marathwada University, Chhatrapati Sambhajinagar. (MS), 431004, India.

^bDepartment of Physics, Deogiri college, Chhatrapati Sambhajinagar. (MS), 431004, India.

Abstract:

This work employed the Sol-gel auto-combustion process to produce ferrite samples of NiCuFe₂O₄ and NiMgFe₂O₄. various analytical methods were used to examine the synthetic materials' structural, optical, and functional groups, including XRD, UV-Vis, and FTIR. Furthermore, we examined the gamma-ray shielding characteristics for the produced materials using a NaI (Tl) scintillation detector and various gamma-ray sources. The theoretical values and the experimental results exhibited a strong connection. This software program evaluated the synthesized ferrite nanoparticles' capability to shield against gamma radiation. By adjusting the radiation dose's strength, ferrites have been exposed to gamma radiation from an array of sources. An investigation of the mass and linear attenuation coefficients, mean free path, half value layer, and tenth value layer, for synthesized spinel ferrites at 122–1330 keV is conducted using Phy-X/PSD software. It is widely recognized that the recommended nanoparticles can aid in improving shielding against γ-radiation.

Keywords: XRD, FTIR, and Radiation shielding parameters.

1) Introduction:

The more technologies that use radiation, the more radiation-protective materials are being developed. Photons with high intensity that might ordinarily cause irreversible injury to human cells are absorbed by these radiation shields. An extended period of high-intensity radiation exposure can lead to severe cases of cancer, illness, tissue damage, and even death [1-3]. When it comes to radiation shields, material diversity offers a multitude of applications and materials to choose from [4–10]. For example, concrete is cheap and easily shaped into different forms, making it a popular material for lining the walls of laboratories and nuclear power plants [11]. Concrete, on the other hand, is prone to breaking over time and blocks your light [12]. Efforts to find a more effective radiation shield have focused on the development of ferrite nanoparticles by researchers.

The most promising material for use in radiation shielding is nanoparticles. Reducing undesired emissions and shielding materials and devices from external radiation are necessary to prevent the harmful effects of radiation on human health [13]. To evaluate the radiation shielding ability of various composite materials, numerous researches have been conducted recently to calculate the parameters of particular attenuation coefficients and γ -ray shielding. In-depth studies of the radiation shielding of cobalt (Co) and zinc (Zn)--based spinel ferrite materials were necessary to examine the previously mentioned point of view. The electrical, magnetic, radiation shielding, and spectral analyses of Mg-doped Ni–Cu–Zn Nanoferrites were conducted by Henaish et al. [14]. They discovered that the 0% sample had the highest Zeff and μ m. Magnesium level rises due to zinc, effectively blocking gamma rays. Mansy et al. [15] examined the attenuation properties of gamma rays and fast neutrons from Ni_xCo_{1-x}Fe₂O₄ nickel ferrites.

Here, the tried-and-true methods such as the sol-gel method yield a homogeneous product with small particles and a wide surface area; moreover, the method is less expensive and takes less time to process. Many efforts have been made to create ferrite nanoparticles that are suitable for use as gamma-ray shielding material; it has been found that the ferrite nanoparticles in NiCuFe₂O₄ and NiMgFe₂O₄ exhibit structural, mechanical, and chemical stability; furthermore, they should work well as gamma and X-ray absorbers. Accordingly, we created NiCuFe₂O₄ and NiMgFe₂O₄ ferrite nanoparticles and in the current work, we examined their gamma radiation shielding capabilities. To our knowledge, the synthesis of NiCuFe₂O₄ and NiMgFe₂O₄ ferrite nanoparticles using the sol-gel method has proven to be a flexible and energy-efficient technique. The fabricated nanoparticles were analyzed using X-ray diffraction (XRD), UV-visible absorption spectroscopy, and Fourier transmission infrared spectroscopy (FTIR). Further research is done on the production of ferrite nanoparticles, NiCuFe₂O₄ and NiMgFe₂O₄, and their gamma-ray shielding capabilities. This research opens up a new path for the simple, economical, and effective production of nanomaterials for gamma-ray shielding.

2) Materials and Method:

Materials for the synthesis of NiCuFe₂O₄ and NiMgFe₂O₄ were prepared ferrite nanoparticles according to this given content of 99.9% pure AR grade ferric nitrate (Fe (NO₃)₃ 9H₂O), nickel nitrate hexahydrate (Ni (NO₃)6H₂O, Cupper (III) nitrate (Cu (NO₃)₂ 3H₂O and magnesium nitrate (Mg (NO₃)₂), were used as starting materials to prepare NiCuFe₂O₄ and NiMgFe₂O₄. Urea [CH₄N₂O] was used as fuel because of its better complexing ability and low ignition temperature (200–250 °C) than other fuels used in wet-chemical methods. Metal nitrate to urea was maintained in a molar ratio of 1:3. A minimum amount of deionized water was mixed with a stoichiometric proportion of metal nitrates to create a homogenous solution. To keep the pH of the combined nitrate solution at 7, it was vigorously agitated using liquid ammonium hydroxide (NH₄OH), drop by drop. For three to four hours, the mixed solution was heated simultaneously at 70 °C to form a sol. To eliminate the water, the transparent sol was heated for one hour at 110 °C. Sol becomes a thick brown gel as the temperature rises. The viscous brown gel turns into a dried gel when it is constantly stirred and heated.

When the gel reached an appropriate temperature, ignition started, and it burned in a self-propagating manner until it was completely burned, forming a fluffy, loose powder that was NiCuFe₂O₄ and NiMgFe₂O₄. After drying, the powder was annealed for 5 hours at 700°C. The prepared powder of loose NiCuFe₂O₄ and NiMgFe₂O₄. ferrite was grinded in a planetary ball mill for 40 minutes, samples were characterized by XRD, FTIR, Uv-Vis, and Radiation parameters by using NaI-(Tl) Scintillation detector [16-20].

3) Result and Discussion

3.1) X-ray Diffraction Analysis

The structural properties of the synthesized ferrite samples, namely S1 (Nickel Copper Ferrite) and S2 (Nickel Magnesium Ferrite), prepared via the sol–gel method, were investigated using X-ray diffraction (XRD). The diffraction patterns of both samples exhibited well-defined peaks at 20 values of 30.26°, 35.64°, 43.33°, 57.31°, and 62.94°, which are characteristic of spinel ferrite structures. These reflections correspond to the crystallographic planes (220), (311), (400), (511), and (440), respectively, and are in good agreement with the standard JCPDS card No. 22–1086 for cubic spinel ferrites, confirming the successful formation of a single-phase spinel structure without any detectable impurity phases[21]. The lattice parameter (a) for both samples was calculated using the relation for cubic systems[22, 23].

$$\frac{1}{d^2} = (h^2 + k^2 + l^2) \frac{1}{c^2}$$

The obtained values were found to be nearly identical, around $\mathbf{a} = 6.92 \, \text{Å}$, which matches well with the reported values for spinel ferrites. This consistency in lattice parameter indicates that the substitution of Cu^{2+} and Mg^{2+} ions in the nickel ferrite lattice does not significantly distort the cubic structure, suggesting successful incorporation of dopant ions within the spinel framework[24]. The average crystallite size (D) was determined using the Debye–Scherrer equation from the most intense diffraction peak (311)[25-27].

$$D = \frac{K\lambda}{\beta cos\theta}$$

The crystallite size of the S1 (Ni–Cu ferrite) sample was estimated to be **33.93 nm**, whereas the S2 (Ni–Mg ferrite) sample showed a smaller size of **20.50 nm**. The observed decrease in crystallite size upon magnesium substitution could be attributed to differences in ionic radii and bonding preferences of Mg²⁺ compared to Cu²⁺, which influences the nucleation and growth process during the sol–gel synthesis[28]. Thus, the XRD results confirm the formation of nanocrystalline spinel ferrite structures with controlled crystallite sizes, which may strongly influence their physical and functional properties for potential applications.

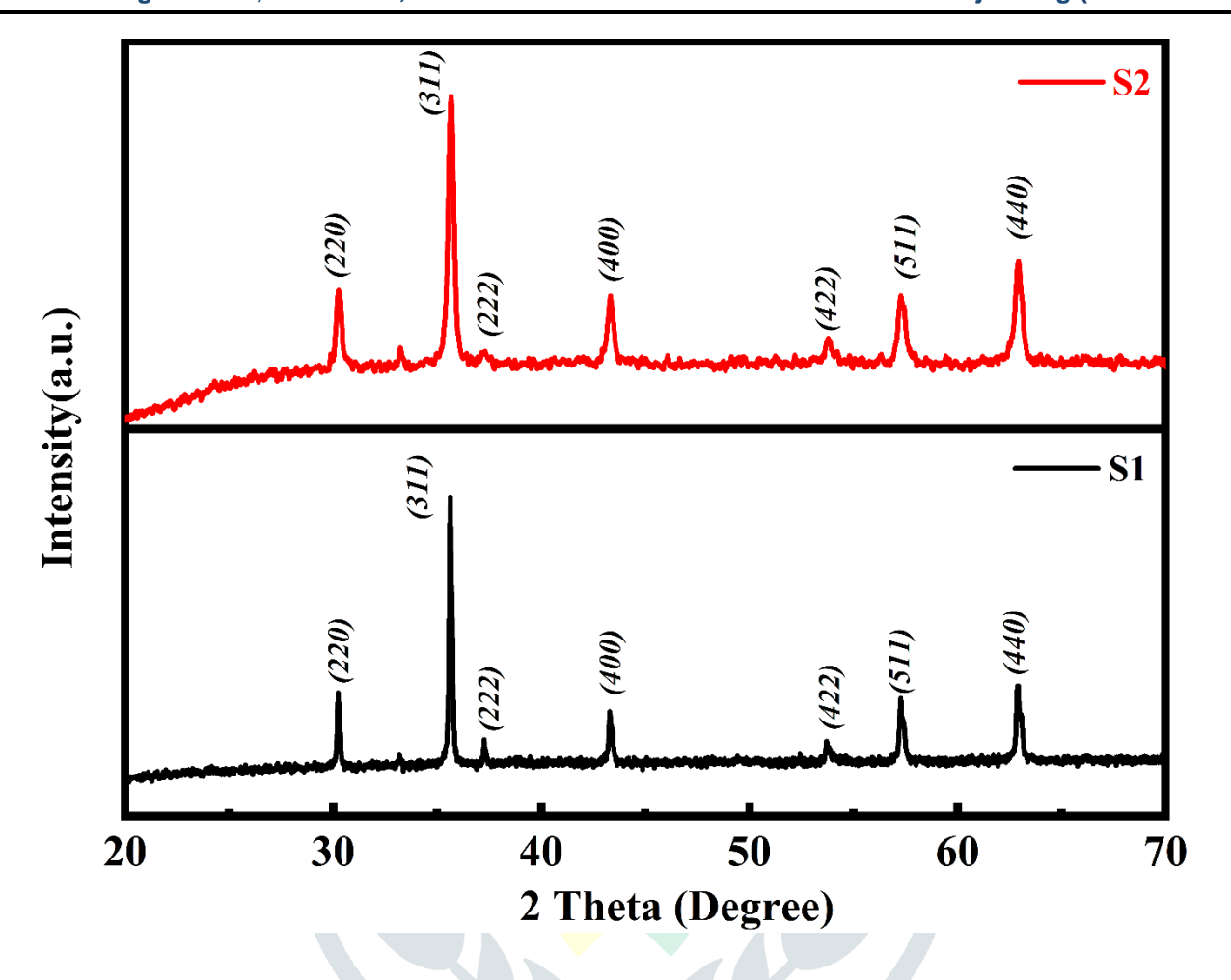


Figure 1 XRD spectra of synthesized samples.

3.2) FTIR Analysis

Fourier Transform Infrared (FTIR) spectroscopy is a powerful tool to confirm the formation of spinel ferrite structures by analysing the characteristic metal—oxygen vibrational bands. In the present study, FTIR spectra of NiFe₂O₄ samples are recorded in the wavenumber region of 4000–300 cm⁻¹. This range is particularly important for ferrite systems, as it reveals the fundamental vibrational modes of metal—oxygen bonds in the crystal lattice. The spectra display two distinct broad absorption bands that are typical features of spinel ferrites. The first absorption band (v₁), appearing in the range of 600–550 cm⁻¹, is attributed to the stretching vibrations of metal—oxygen bonds located at the tetrahedral sites of the spinel structure[29]. The second band (v₂), generally observed in the range of 450–385 cm⁻¹, corresponds to the vibrations of metal—oxygen bonds at the octahedral sites[30]. The presence of these two well-defined absorption bands in all investigated samples confirms the formation of the spinel phase, as they reflect the characteristic distribution of cations over tetrahedral and octahedral interstitial positions. Thus, FTIR analysis not only verifies the spinel structure of NiFe₂O₄ but also provides insight into the bonding nature and cationic environment within the lattice, supporting the structural results obtained from XRD analysis.

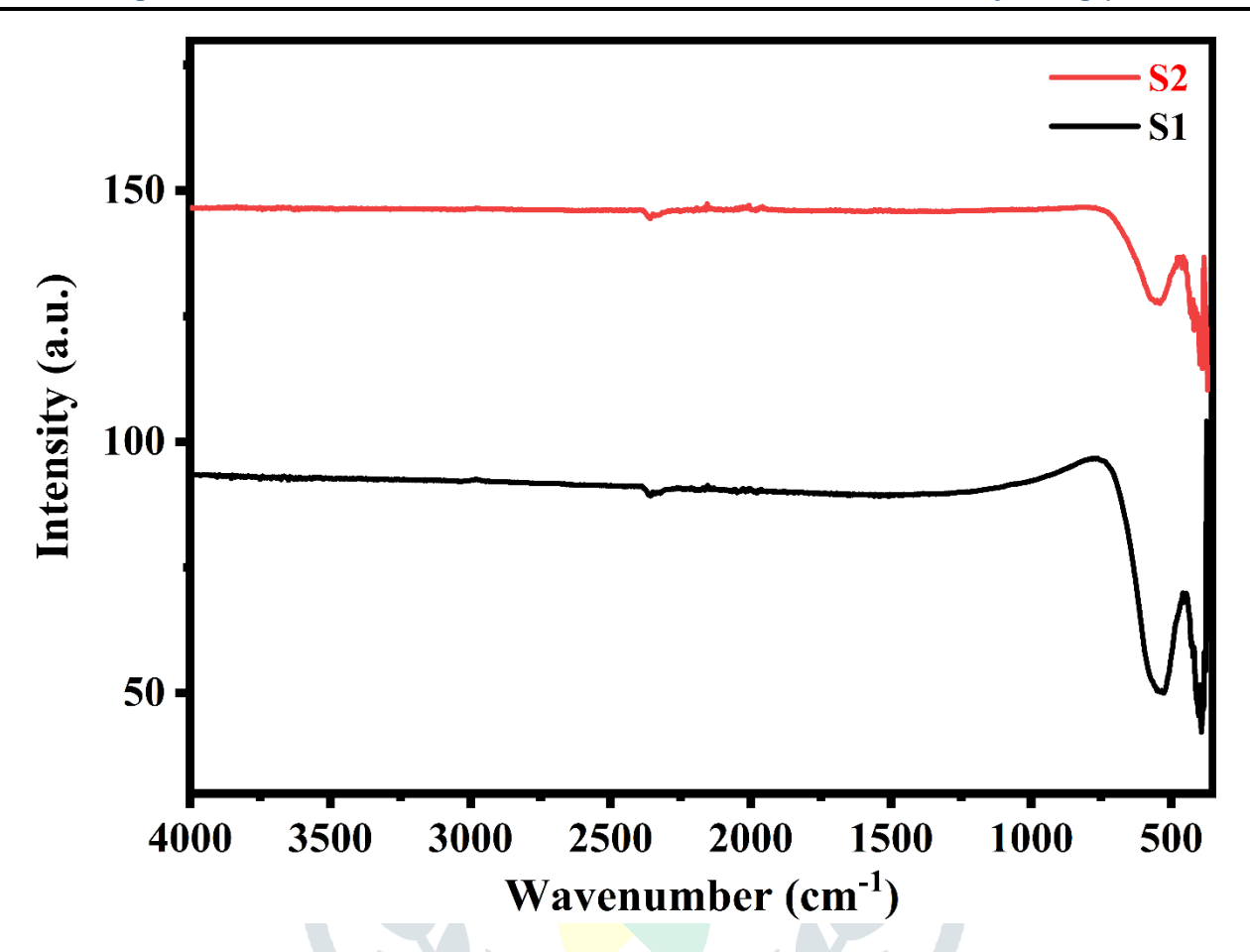


Figure 2 FTIR spectra of synthesized samples.

3.3 Optical Property Study

The optical properties of ferrite nanoparticles can be studied using UV–Vis spectroscopy, which provides insight into their electronic band structure shown[31]. Figure 3 shows the absorption spectra of the prepared S1 (Nickel Copper Ferrite) and S2 (Nickel Magnesium Ferrite) samples. The band gap energies were determined using the Tauc plot method[32, 33].

$$\alpha h \upsilon = A(h \upsilon - E_g)^n$$

For S1, the estimated optical band gap is 2.84 eV, while for S2 it is 3.24 eV. The difference in band gap values can be attributed to the nature of the substituted cations (Cu²⁺ in S1 and Mg²⁺ in S2) and their influence on the electronic structure of the spinel ferrite lattice.

In Nickel Copper Ferrite (S1), the incorporation of Cu²⁺ ions, which possess partially filled d-orbitals, introduces localized electronic states within the band structure[34]. These states effectively reduce the energy difference between the valence and conduction bands, leading to a narrower band gap (2.84 eV). Such a reduced band gap enhances visible-light absorption and can improve photocatalytic and optoelectronic properties[35]. In contrast, Nickel Magnesium Ferrite (S2) exhibits a larger band gap of 3.24 eV. This is because Mg²⁺ ions are non-transition metal cations with no d-electrons, and their substitution does not create

additional localized states in the band structure[36]. As a result, the material maintains a wider separation between the valence and conduction bands. The larger band gap makes S2 more suitable for applications requiring higher-energy photon absorption, such as UV-light-driven processes. Thus, the observed band gap variation between S1 and S2 highlights the role of cation substitution in tuning the optical properties of ferrite nanomaterials for specific applications[37-43].

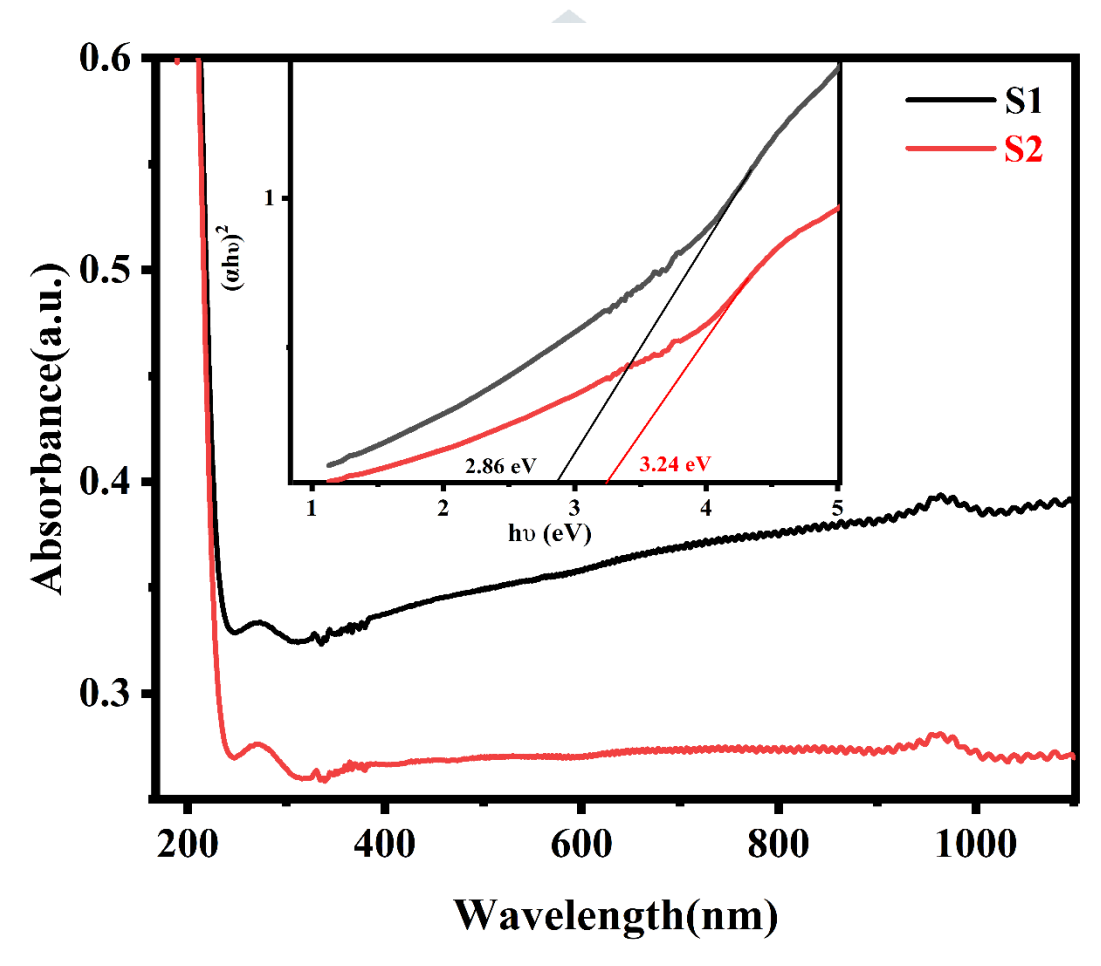


Figure 3 UV-Vis absorption spectra and Tauc plot of synthesized samples.

3.4) Radiation Shielding Properties:

The theoretical MAC was computed using the Phy-X/PSD algorithm, and the results were compared to the experimental data. Phy-X/PSD software was used to estimate additional properties. Several researchers used this software to assess the radiation shielding capabilities of various materials, such as glasses [38]. Linear attenuation coefficients (LAC), Mass attenuation coefficients (MAC), half-value length (HVL), tenth-value length (TVL), and mean free path (MFP).

3.4.1. Linear Attenuation Coefficient (LAC)

Figure 4 shows the linear attenuation coefficient (μ) of a particular ferrite nanoparticle to energy. It is possible to see how the linear attenuation coefficient for all created samples drops exponentially as energy is increased. Sample S2 has the lowest LAC value, whereas Sample S1 has the highest. Furthermore, the S2 ferrite decays

faster than the spinel ferrites selected in the energy range of 122 to 356 keV, after which it drops linearly with energy. A linear attenuation coefficient is a key factor when evaluating a material's shielding performance [39].

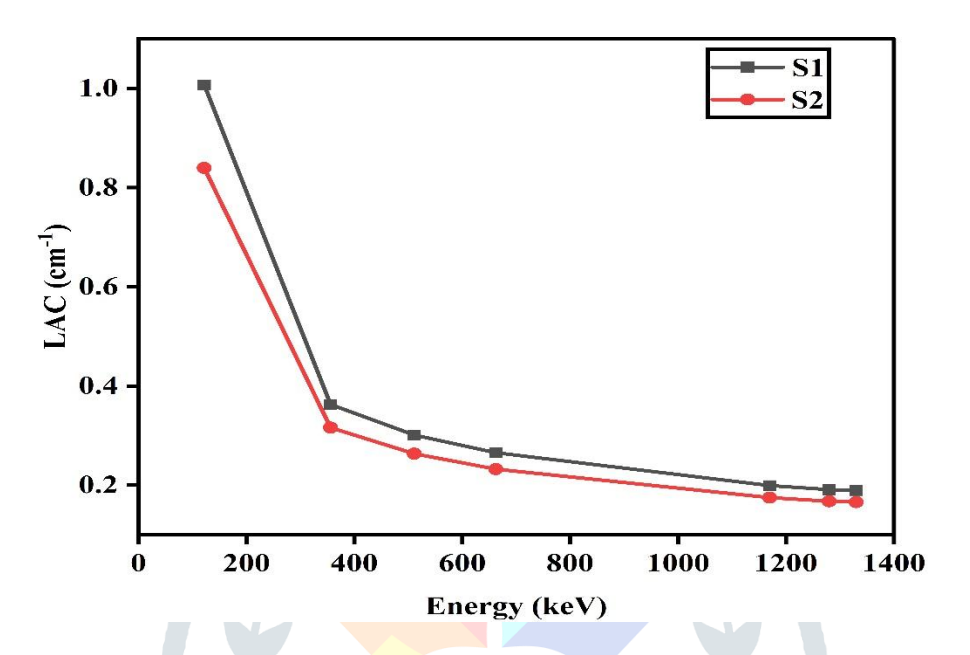


Figure. 4. Linear Attenuation Coefficient (LAC) of the synthesized sample.

3.4.2. Mass Attenuation Coefficient (MAC)

Figure 5 and Table 1 display mass-attenuation coefficients for nano and micro-sized NiCuFe₂O₄ and NiMgFe₂O₄ ferrites Nanoparticles. The results from experimental measurements and Phy-X are nearly equivalent, with tiny variation values not exceeding 4.0%. This finding shows that the size of the nickel magnesium ferrite has little effect on the attenuation qualities. The S1 composition had the largest mass-attenuation coefficients at different energies because to its high NiCuFe₂O₄ content, while NiMgFe₂O₄ had the lowest due to its high Mg content. The accuracy and consistency of the results obtained by Phy-X are notable, confirming the validation of its application in computing the mass-attenuation coefficient for micro-sized materials [44]

Table 1. Comparison of Theoretical (Phy-X) and Experimental Mass Attenuation Coefficient.

Energy	Phy-X S1	Exp	% Dev	Phy-X S2	Exp	% Dev
122	0.2799	0.2764	1.263199318	0.2678	0.2636	1.564052437
356	0.1016	0.0978	3.701091942	0.1008	0.0962	4.519178853
511	0.0836	0.0818	2.18304748	0.0839	0.0822	2.055994396
662	0.0737	0.0722	2.011775266	0.0740	0.0729	1.54595148
1170	0.0553	0.0539	2.582160106	0.0557	0.0541	2.820999791
1280	0.0530	0.0512	3.459772736	0.0534	0.0517	3.116982282
1330	0.0525	0.0507	3.496832703	0.0529	0.0511	3.333798104

The MAC of S1 and S2 ferrites can be determined using its assistance. To demonstrate how the findings in Table 1 differ in percentage. This figure validates the experiment that was used to produce the MAC values. Figure 7 depicts the mass attenuation coefficient values for various samples in the energy range of 122 keV to 1330 keV. At 122 keV, MAC is 0.2799 cm²/g for S1 and 0.2496 cm²/g for S2, while at 1330 keV, it is 0.0525cm²/g, and 0.0529 cm²/g, respectively.

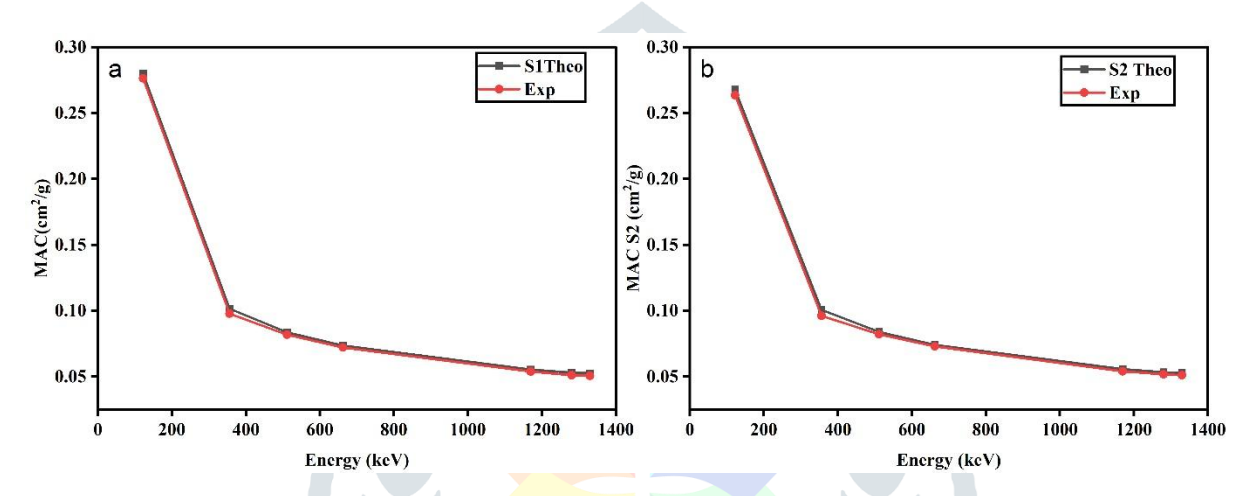


Figure. 5. Comparison of theoretical and experimental results of Mass Attenuation Coefficient (MAC) synthesized sample.

3.4.3 Mean Free Path (MFP)

Figure 6 depicts the ferrite nanoparticles' mean free path (MFP). The MFP value is found at the lowest tested energy, 122 keV, and ranges from 1.1908 to 0.9928 cm. At 1330 keV, the largest MFP is discovered to be between 5.2899 and 6.0324cm. Because higher intensity radiation can easily flow through the damaged material, there is a growing tendency in the MFP. At higher energies, the Compton interaction replaces the photoelectric effect [45-47]. Since this alteration, photon attenuation has decreased because the Compton interaction, which is generally independent of atomic number and energy, happens mostly between incoming photons and the outer shell electron of an atom within ferrite nanoparticles.

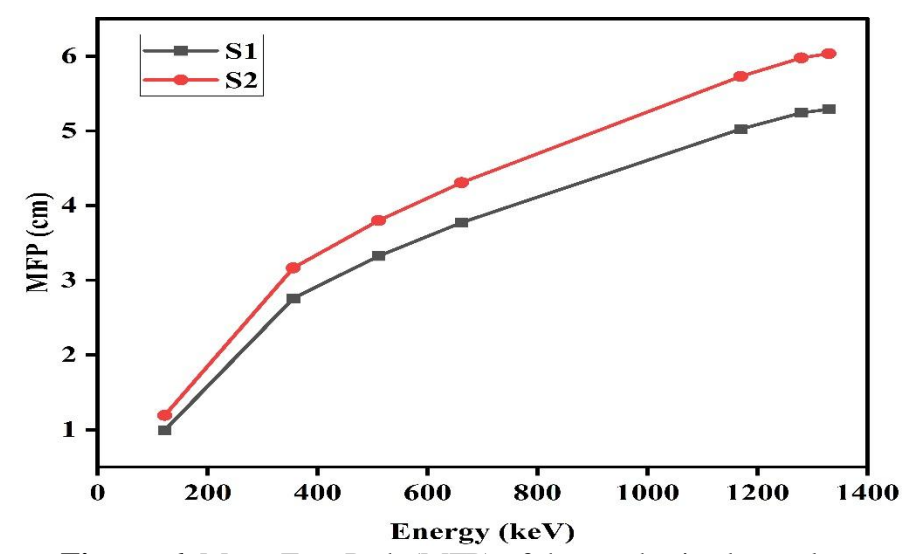


Figure. 6. Mean Free Path (MFP) of the synthesized sample.

3.4.4 Half Value Layer (HVL) and Tenth Value Layer (TVL)

Figures 7 and 8 depict the Half Value Layer and Tenth Value Layer, respectively. The HVL values for a given energy are organized in the following order, and they rise when energy levels S2 > S1. In other words, the S1 sample has the lowest HVL and the best shielding ability, whereas the S2 sample has the highest HVL but the lowest acceptable shielding capacity. In addition, the influence of energy on HVL was investigated. There is evidence that HVL increases with higher energy levels. The HVL of the S1 sample grew from 0.6881 to 1.9119, 2.3036, 2.6144, 3.4817, 3.6323, and 3.6667 cm at energies of 122, 356, 511, 662, 1170, 1275, and 1330 keV, respectively. Higher energy photons are more likely to pass through nanoparticles and impact with material atoms less frequently, causing HVL to rise and remain. As a result, the space efficiency of nanoferrites increases at lower energies while decreasing at higher energies [48-51]. Similar results show the TVL outcomes as the HVL

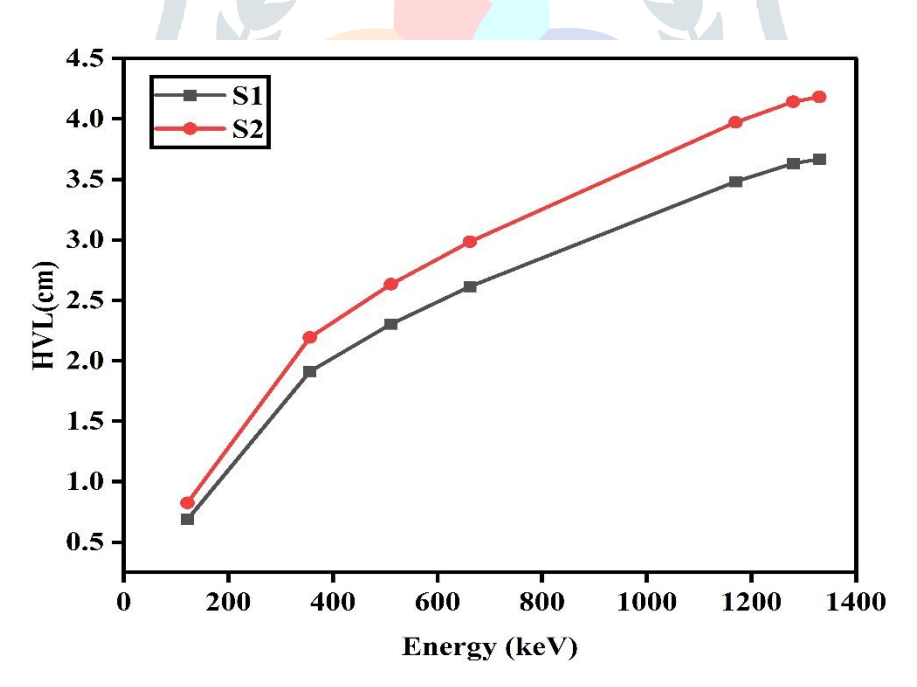


Figure. 7. Half Value Layer (TVL) of the synthesized sample.

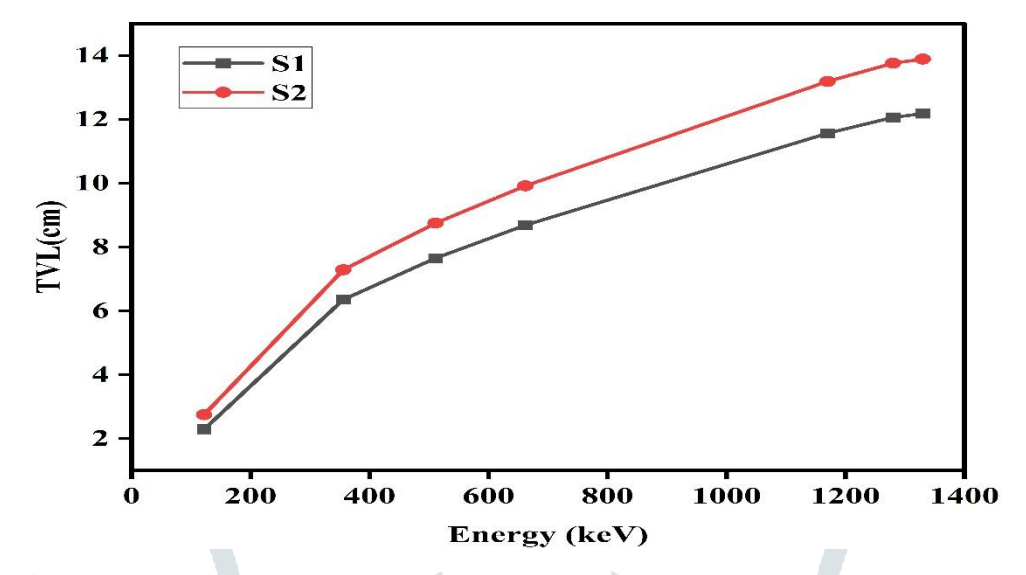


Figure. 8. Experimental Tenth Value Layer (TVL) of the synthesized sample.

4) Conclusion:

This study looked at the radiation shielding properties of NiCuFe₂O₄ and NiMgFe₂O₄ nanoparticles. to determine how effective photon protection is. The computations in the study were done using Phy-X/PSD. LAC, MAC, TVL, and HVL. The mass attenuation coefficient was experimentally determined for each ferrite nanoparticle sample using the Phy-X/PSD program and the NaI (Tl) scintillation detector. Furthermore, HVL values for a given energy are grouped in the following order, and they increase when energy levels S2 > S1. These numbers rise in lockstep with the energy levels. Alternatively, the S1 sample has the lowest HVL and the best shielding capacity, whereas the S2 sample has the highest HVL and the least effective shielding capacity. This shows how ferrite nanoparticle samples can be employed in radiation-safe applications. Future research could lead to the development of more effective radiation barrier materials. The study results can be used as a first approximation and as the foundation for future investigations.

5) References:

- 1. H.O. Tekin, Shams A.M. Issa, K.A. Mahmoud, F.I. El-Agawany, Y.S. Rammah, G. Susoy, M.S. Al-Buriahi, Mohamed M. Abuzaid, I. Akkurt, Nuclear radiation shielding competences of Barium (Ba) reinforced borosilicate glasses, Emerg. Mater. Res. 9e4 (2020).
- 2. Yonca Yahs, i Çelen, Atilla Evcin, Synthesis and characterizations of magnetiteeborogypsum for radiation shielding, Emerg. Mater. Res. 9e3 (2020) 770e775,
- 3. Feride Kulali, Simulation studies on the radiological parameters of marble concrete, Emerg. Mater. Res. (2020).
- 4. S.S. Obaid, M.I. Sayyed, D.K. Gaikwad, P.P. Pawar, Attenuation coefficients and exposure buildup factor of some rocks for gamma ray shielding applications, Radiat. Phys. Chem. 148 (2018) 86e94.

- 5. S.S. Obaid, M.I. Sayyed, D.K. Gaikwad, H.O. Tekin, Y. Elmahroug, P.P. Pawar, Photon attenuation coefficients of different rock samples using MCNPX, Geant4 simulation codes and experimental results: a comparison study, Radiat. Eff. Defect Solid 173 (2018) 900e914.
- D.K. Gaikwad, M.I. Sayyed, S.N. Botewad, S.S. Obaid, Z.Y. Khattari, U.P. Gawai, F. Afaneh, M.D. Shirshat, P.P. Pawar, Physical, structural, optical investigation and shielding features of tungsten bismuth tellurite-based glasses, J. NonCryst. Solids 503e504 (2019) 158e168.
- 7. S.S. Obaid, D.K. Gaikwad, P.P. Pawar, Determination of gamma ray shielding parameters of rocks and concrete, Radiat. Phys. Chem. 144 (2018) 356e360.
- 8. Iskender Akkurt, Effective atomic and electron numbers of some steels at different energies, Ann. Nucl. Energy 36e11 (12) (2009) 1702e1705.
- 9. Yasser Saad Rammah, Ashok Kumar, Karem Abdel-Azeem Mahmoud, Raouf El-Mallawany, Fouad Ismail El-Agawany, Gulfem Susoy, Huseyin Ozan Tekin, SnO-reinforced silicate glasses and utilization in gamma radiation-shielding applications, Energy. Mater. Res. 9e3 (2020) 1000e1008.
- 10. Roya Boodaghi Malidarrea, Feride Kulali, Aysun Inal, Oz Ali, Monte Carlo simulation of the Waste Soda-Lime-Silica Glass system contained Sb2O3, Emerg. Mater. Res. (2020)
- 11. A. Mahmoud, O.L. Tashlykov, A.F. El Wakil, H.M.H. Zakaly, I.E. El Aassy, Investigation of radiation shielding properties for some building materials reinforced by basalt powder, AIP Conf. Proc. (2019) 2174.
- 12. A.S. Abouhaswa, M.I. Sayyed, A.S. Altowyan, Y. Al-Hadeethi, K.A. Mahmoud, Synthesis, structural, optical and radiation shielding features of tungsten trioxides doped borate glasses using Monte Carlo simulation and phy-X program, J. Non-Cryst. Solids 543 (2020) 120134,
- 13. N.N. Ali, Y. Atassi, A. Salloum, A. Charba, A. Malki, M. Jafarian, Mater. Chem. Phys. 211 (2018) 79.
- 14. S.S. Obaid, M.I. Sayyed, D.K. Gaikwad, P.P. Pawar, Attenuation coefficients and exposure buildup factor of some rocks for gamma ray shielding applications, Radiat. Phys. Chem. 148 (2018) 86e94.
- 15. S.S. Obaid, M.I. Sayyed, D.K. Gaikwad, H.O. Tekin, Y. Elmahroug, P.P. Pawar, Photon attenuation coefficients of different rock samples using MCNPX, Geant4 simulation codes and experimental results: a comparison study, Radiat. Eff. Defect Solid 173 (2018) 900e914.
- 16. A. Mahmoud, O.L. Tashlykov, A.F. El Wakil, H.M.H. Zakaly, I.E. El Aassy, Investigation of radiation shielding properties for some building materials reinforced by basalt powder, AIP Conf. Proc. (2019) 2174.
- 17. A.S. Abouhaswa, M.I. Sayyed, A.S. Altowyan, Y. Al-Hadeethi, K.A. Mahmoud, Synthesis, structural, optical and radiation shielding features of tungsten trioxides doped borate glasses using Monte Carlo simulation and phy-X program, J. Non-Cryst. Solids 543 (2020) 120134,
- 18. N.N. Ali, Y. Atassi, A. Salloum, A. Charba, A. Malki, M. Jafarian, Mater. Chem. Phys. 211 (2018) 79.
- 19. Y. Zhan, Z. Long, X. Wan, J. Zhang, S. He, Y. He, Appl. Surf. Sci. 444 (2018) 710.
- 20. J. Ma, X. Wang, W. Cao, C. Han, H. Yang, J. Yuan, M. Cao, Chem. Eng. J. 339 (2018)

q529

- 21. Rao DH, Dhanalakshmi B, Dasari M. Sol-Gel synthesized structural, microstructural and magnetic studies on Dy and Mn co-doped Co(1-x)DyxFe(2-y)MnyO4 nanoparticles. Journal of the Indian Chemical Society. 2025;102(1):101542.
- 22. Mane VA, Dake DV, Raskar ND, Sonpir RB, Stathatos E, Dole BN. Magneto-optical properties of Fedoped bismuth oxide nanorods for photocatalytic and antimicrobial applications. Results in Chemistry. 2023; 6:101083.
- 23. Mane VA, Dake DV, Raskar ND, Sonpir RB, Stathatos E, Dole BN. Growth in defects and surface area for the photocatalytic performance of GO-based Fe-doped bismuth oxide mesoporous nanocomposite. Ceramics International. 2024;50(7, Part A):11179-89.
- 24. Sultana S, Rahman MN, Hossain MA, Rahman MR. Cation concentration effects on structural, morphological, and magnetic behavior of CoMg_{0.5}Fe_{1.5}O₄ via reverse annealing. Next Materials. 2025; 9:101104.
- 25. Mane VA, Dake DV, Raskar ND, Sonpir RB, Gattu KP, Shirsat MD, et al. Harnessing the synergistic effects of graphene oxide-based Sn/Fe codoped Bi2O3 nanocomposites for superior supercapacitor performance. Journal of Energy Storage. 2024; 96:112636.
- 26. Mane VA, Dake DV, Raskar ND, Sonpir RB, Vasundhara M, Dole BN. Nanointerface engineering of MXene based Fe doped Bi2O3 nano heterostructures for efficient energy storage and environmental remediation. Journal of Energy Storage. 2025; 111:115425.
- 27. Mane VA, Dake DV, Raskar ND, Sonpir RB, Chavan KM, Gattu KP, et al. Multifunctional Fe-Doped Bi2O3/TiO2 heterojunctions for environmental remediation and gas sensing. Surfaces and Interfaces. 2025; 58:105908.
- 28. Ikram S, Ashraf F, Alzaid M, Mahmood K, Amin N, Haider S. Role of Nature of Rare Earth Ion Dopants on Structural, Spectral, and Magnetic Properties in Spinel Ferrites. Journal of Superconductivity and Novel Magnetism. 2021; 34:1-7.
- 29. Rathod V, A V A, Kumar R, Jali V, Sahoo DB. Correlated vibrations of the tetrahedral and octahedral complexes and splitting of the absorption bands in FTIR spectra of Li-Zn ferrites. Vibrational Spectroscopy. 2017; 92:267-73.
- 30. Xian G, Kong S, Li Q, Zhang G, Zhou N, Du H, et al. Synthesis of Spinel Ferrite MFe2O4 (M = Co, Cu, Mn, and Zn) for Persulfate Activation to Remove Aqueous Organics: Effects of M-Site Metal and Synthetic Method. Frontiers in Chemistry. 2020;8.
- 31. Makrand E Sonawane, Vishnu V Kutwade, Dipak A Tonpe, Khan Faizan Mazher, Prakash Gajbar, Shaikh Sumaiyya, Ramphal Sharma, Numerical study of buffer layers to obtain high performance solar cell, International Journal of Modern Physics B,39,2550155
- 32. Makrand E Sonawane, Ketan P Gattu, Vishnu V Kutwade, Dipak A Tonpe, Faizan M Khan, Sumaiyya Shaikh, Prakash S Gajbar, Ramphal B Sharma, Ni doping in CZTS solar cells: a path to enhanced photovoltaic performance, Indian Journal of Physics, 99,1133-1143

- 33. Prakash S Gajbar, Shankar S Humbe, Makrand E Sonawane, Ketan P Gattu, Dipak A Tonpe, Vishnu V Kutwade, Faizan M Khan, Shaikh Sumaiyya Firdous, Ramphal Sharma, Structural and optoelectronic properties of CuS nano particles prepared by Co-precipitation method, International Journal of Modern Physics B, 2550148
- 34. Hossain I, Islam MT, Mohd Sahar N, Samsuzzaman M, Alzamil A, Soliman MS. Structural, morphological, optical and electrical properties of ferrite-based nanoparticles synthesized flexible substrate for chemical sensing application. Journal of Science: Advanced Materials and Devices. 2024;9(3):100750.
- 35. Mane VA, Dake DV, Raskar ND, Sonpir RB, Shirsat MD, Dole BN. Optimization, kinetic analysis, and photocatalytic degradation of rhodamine B using manganese doped nanoscale nickel oxide nanoparticles. Ceramics International. 2024;50(20, Part B):38871-83.
- 36. Makrand E Sonawane, Ketan P Gattu, Vishnu V Kutwade, Dipak A Tonpe, Ramphal Sharma, Optoelectronic characteristics of microwave-synthesized cobalt-doped CZTS for solar cell absorber layers, 3198, AIP Conference Proceedings, 020041
- 37. Makrand E Sonawane, Ketan P Gattu, Dipak A Tonpe, Vishnu V Kutwade, Ibrahim MS Mohammed, Faizan M Khan, Prakash S Gajbar, Sumaiyya F Shaikh, Ramphal B Sharma, MoS2 augmentation in CZTS solar cells: Detailed experimental and simulation analysis, 39, Nano-Structures & Nano-Objects, 101268
- 38. Dipak A Tonpe, Ketan P Gattu, Vishnu V Kutwade, Makrand E Sonawane, Mahesh C Sharma, Hyungil Jang, Sung-Hwan Han, Ramphal Sharma, ZnS-PANI nanocomposite with enhanced electrochemical performances for lithium-ion batteries, Journal of Materials Science: Materials in Electronics, 33, 18452-18463
- 39. Mane VA, Dake DV, Raskar ND, Sonpir RB, Dole BN. Synergistic Enhancement of Photocatalytic and Antifungal Activities in Microwave-Assisted ZnO/Fe-Doped Bi2O3 Nanocomposites. physica status solidi (a). 2024;221(9):2300954.
- 40. Ghosh M, Datta S, Sharma R, Tanbir K, Kar M, Mukherjee S. Copper doped nickel ferrite nanoparticles: Jahn-Teller distortion and its effect on microstructural, magnetic and electronic properties. Materials Science and Engineering B. 2021;263:114864.
- 41. Casbeer E, Sharma VK, Li X-Z. Synthesis and photocatalytic activity of ferrites under visible light: A review. Separation and Purification Technology. 2012; 87:1-14.
- 42. Singh N, Agarwal A, Sanghi S, Singh P. Effect of magnesium substitution on dielectric and magnetic properties of Ni–Zn ferrite. Physica B-condensed Matter PHYSICA B. 2011; 406:687-92.
- 43. Ahmed M, Zheng Y, Wang G, Chen G. Nanostructured spinel ferrites: A comprehensive study on the synthesis, characterization, and magnetic properties of Zn and Mn substituted magnetite nanoparticles produced through the co-precipitation method. Journal of Materials Research and Technology. 2024; 33:5987-6010.

- 44. Kalidas B. Gaikwad, Ketan P. Gattu, Chaitali V. More, Pravina P. Pawar, Physical, structural and nuclear radiation shielding behaviour of Ni–Cu–Zn Fe2O4 ferrite nanoparticles, Applied Radiation and Isotopes, 207, (2024), 111244.
- 45. Muhammad S. Mansy, W.M. Desoky, Investigation of gamma-rays and fast neutrons attenuation parameters for Ni_xCo_{1-x}Fe₂O₄ nickel ferrites, Progress in Nuclear Energy 148 (2022) 104213.
- 46. Kalidas B. Gaikwad, Ketan P. Gattu, Shamsan S. Obaid, Pravina P. Pawar, Comparative study of radiation shielding parameters for NiFe₂O₄ and CoFe₂O₄ nanoparticles, AIP Conf. Proc. 3149, 020014 (2024).
- 47. H.O. Tekin, Shams A.M. Issa, K.A. Mahmoud, F.I. El-Agawany, Y.S. Rammah, G. Susoy, M.S. Al-Buriahi, Mohamed M. Abuzaid, I. Akkurt, Nuclear radiation shielding competences of Barium (Ba) reinforced borosilicate glasses, Emerg. Mater. Res. 9e4 (2020).
- 48. Yonca Yahs, i Çelen, Atilla Evcin, Synthesis and characterizations of magnetiteeborogypsum for radiation shielding, Emerg. Mater. Res. 9e3 (2020) 770e775,
- 49. Kalidas B. Gaikwad, Ketan P. Gattu, Chaitali V. More, Hasan Ogul, Pravina P. Pawar, Gamma-ray shielding features of Co_{1-x}Cu_xFe₂O₄ ferrite: A combined experimental, theoretical and simulation investigation, Radiation Physics and Chemistry, 224, 111996, (2024).
- 50. Kalidas B. Gaikwad, Ketan P. Gattu, Chaitali V. More, M.I. Sayyed, Kanchan R. Niras, Pravina P. Pawar, Experimental evaluation of gamma radiation attenuation properties of Ni_{0.2}Mg_xZn_{0.8}-_xFe₂O₄, Optical Materials 148 (2024) 114807.
- 51. Kalidas B Gaikwad, Merfat Algethami, Chaitali V More, MI Sayyed, Pravina P Pawar, Enhanced radiation shielding properties of advanced ceramic materials, Journal of Alloys and Compounds Volume 1033, 20 June 2025, 181384.